Ultrasoft primitive model of polyionic solutions: Structure, aggregation, and dynamics

Daniele Coslovich,[1,a)] Jean-Pierre Hansen,[2] and Gerhard Kahl[3]

[1]*Laboratoire Charles Coulomb UMR 5221, Université Montpellier 2 and CNRS, Montpellier, France*
[2]*Department of Chemistry, University of Cambridge, Cambridge, United Kingdom and PECSA, Université Pierre et Marie Curie, Paris, France*
[3]*Institut für Theoretische Physik and Center for Computational Materials Science (CMS), Technische Universität Wien, Wien, Austria*

We introduce an ultrasoft core model of interpenetrating polycations and polyanions, with continuous Gaussian charge distributions, to investigate polyelectrolyte aggregation in dilute and semi-dilute salt-free solutions. The model is studied by a combination of approximate theories (random phase approximation and hypernetted chain theory) and numerical simulations. The calculated pair structure, thermodynamics, phase diagram, and polyion dynamics of the symmetric version of the model (the "ultrasoft restricted primitive model" or UPRM) differ from the corresponding properties of the widely studied "restricted primitive model" (RPM) where ions have hard cores. At sufficiently low temperatures and densities, oppositely charged polyions form weakly interacting, polarizable neutral pairs. The clustering probabilities, dielectric behavior, and electrical conductivity point to a line of sharp conductor-insulator transitions in the density-temperature plane. At very low temperatures, the conductor-insulator transition line terminates near the top of a first order coexistence curve separating a high-density liquid phase from a low-density vapor phase. The simulation data hint at a tricritical behavior, reminiscent of that observed for the two-dimensional Coulomb gas, which contrasts with the Ising criticality of its three-dimensional counterpart, the RPM. © *2011 American Institute of Physics*. [doi:10.1063/1.3602469]

I. INTRODUCTION

Ever since the pioneering work of Gouy,[1] Chapman,[2] and Debye and Hückel,[3] electrostatic interactions are known to play a dominant role in determining the structure, dynamics, and phase behavior of ionic liquids and solutions, as well as in governing the colloid stability of polyelectrolyte solutions, complex biomolecular assemblies, and related soft matter systems. In the case of solutions and melts of microscopic cations and anions (microions), such as Na^+ and Cl^-, a widely studied model system is the primitive model (PM) of oppositely charged hard spheres, which is now known to undergo a phase separation into a very dilute phase of mostly paired ions ("Bjerrum pairs," Ref. 4) and a more concentrated solution of non-aggregated ions, for sufficiently strong Coulomb coupling;[5] for a review of simulation work, see Ref. 6.

Moving to the mesoscopic scale, charged colloidal particles (macroions) are stabilized in aqueous dispersions by the formation of electric double layers of microscopic co- and counterions, leading to a screened Coulombic repulsion between equally charged, "dressed" colloids; for an overview see Ref. 7. Despite this purely repulsive effective interaction between colloids, the so-called "volume terms," associated with the self energy of individual electric double layers, induce a phase separation between dilute and concentrated colloidal dispersions,[8] which may be regarded as the highly

asymmetric counterpart of the fluid-fluid transition of the PM.[5,6] Recently, the experimental and theoretical attention has shifted to the rich phase behavior of "colloidal electrolytes," where the polyanions and polycations are highly charged, hard colloidal,[9] or nanometric particles,[10,11] usually in the presence of added salt.[12–14] These mesoscopic electrolytes may thus be regarded as a generalization of the PM, where the pure Coulombic interactions are replaced by screened repulsive and attractive electrostatic (or Yukawa) forces.

Another important class of complex ionic systems are synthetic or natural polyelectrolytes, i.e., solutions of charged polymer chains,[15] where overall charge neutrality is ensured by either microscopic or mesoscopic counterions. The latter case corresponds to a binary system of polymeric polyanions and polycations, which have been shown to aggregate into neutral or charged polyelectrolyte complexes (complex coacervation), in the presence or absence of added salt.[16–19] Since polyions are now flexible and worm-like charged objects, they cannot be reasonably modeled by charged hard spheres (such as their colloidal counterparts), unless they collapse into quasi-spherical globules like certain folded proteins (e.g., lysozyme). Modern theoretical descriptions of polyelectrolyte complexation are usually based on statistical field-theoretic formulations,[20,21] within a perturbative[22] or a simulation[23] framework.

In the present paper, we introduce and investigate a simple model of polyanion/polycation aggregation in polyelectrolyte solutions without added salt. Swollen polymer coils

---

a)Author to whom correspondence should be addressed. Electronic mail: daniele.coslovich@univ-montp2.fr.

in good solvent are known to interpenetrate easily. In fact, the free energy penalty for two self-avoiding polymer coils to fully overlap, such that their centers of mass (CM's) coincide, is of the order of twice the thermal energy $k_B T$, independent of molecular weight.[24–26] A convenient coarse-grained representation of dilute and semi-dilute polymer coils in good solvent reduces the coils to ultrasoft, interpenetrating particles; the effective pair potentials between CM's of interpenetrating coils can be extracted from full monomer Monte Carlo (MC) simulations of the underlying microscopic model by a systematic inversion procedure.[25, 26] The resulting pair potential is well represented by a Gaussian of amplitude $\simeq 2k_B T$, and width of the order of the radius of gyration, R_g, of the polymer coils.[25, 26] Here, we generalize the ultrasoft core representation to globally neutral binary solutions of polyanions and polycations in a dielectric continuum representing the solvent. The total charge of each polyion is assumed to be smeared over the volume of the coil according to a quenched Gaussian distribution of width R_g, centered on the coil CM, ensuring that the total electrostatic interaction between two coils of equal or opposite signs remains finite, even at full overlap. In particular, the "Coulomb collapse" of oppositely charged ions, which is prevented by the presence of the hard core in the PM, is bypassed in the present model of oppositely charged polyelectrolytes by averaging over the spatial extension of the polyion charge distributions.

In Secs. II–V, we investigate the pair structure, thermodynamics, dielectric behavior, and polyion dynamics of this "ultrasoft primitive model" (UPM) by a combination of approximation schemes borrowed from the theory of ionic liquids, and of Monte Carlo and molecular dynamics (MD) simulations. Special emphasis is laid on the static and dynamic characterization of the polyion aggregation and complexation, which are expected to induce a conductor-insulator (CI) transition at low temperatures and concentrations and eventually to phase separation as in the case of the PM.[5, 6, 27, 28] The complete phase diagram of the symmetric version of the UPM (the "restricted" UPM or URPM), which differs considerably from that of the RPM, will be presented in a subsequent paper. A preliminary account of parts of this work was published elsewhere.[29]

II. THE MODEL

We consider a binary system of N_+ polycations of charge $Q_+ = Z_+ e$ and N_- polyanions of charge $Q_- = Z_- e$ (where e is the proton charge), moving in a dielectric continuum of dielectric permittivity ϵ' (the "solvent" in its "primitive" representation) and confined to a volume V. If $n_\alpha = N_\alpha / V$ ($\alpha = +, -$) are the corresponding number densities, overall charge neutrality requires that

$$Z_+ n_+ + Z_- n_- = 0, \tag{1}$$

while the total polyion number density is $n = n_+ + n_-$. Since the system under consideration is supposed to be a model for polyelectrolyte coils, the polyions are not point particles, but their charges are smeared over a volume of the order of the cube of their radius of gyration (R_{g+} or R_{g-}), according to a Gaussian charge distribution centered on the position $\mathbf{r}_i$ of

the CM of each polyion ($1 \le i \le N = N_+ + N_-$). If r is the distance relative to that position, the normalized charge distribution in units of e of a polyion is assumed to be $Z_\alpha \rho_\alpha(r)$, where

$$\rho_\alpha(r) = \left(\frac{1}{2\pi \sigma_\alpha^2}\right)^{3/2} \exp\left[-r^2/2\sigma_\alpha^2\right], \tag{2}$$

with σ_α of the order of $R_{g\alpha}$ and $\alpha = +, -$; its Fourier transform is

$$\hat{\rho}_\alpha(k) = \int e^{i\mathbf{k}\mathbf{r}} \rho_\alpha(\mathbf{r}) d\mathbf{r} = \exp[-k^2\sigma^2/2]. \tag{3}$$

The electrostatic potential $\varphi_\alpha(r)$ generated by the above charge distribution obeys Poisson's equation (in esu)

$$\nabla^2 \varphi_\alpha(r) = -\frac{4\pi Z_\alpha e}{\epsilon'} \rho_\alpha(r). \tag{4}$$

Taking Fourier transforms of both sides, and remembering Eq. (3), one finds

$$\hat{\varphi}_\alpha(k) = \frac{4\pi Z_\alpha e}{\epsilon' k^2} \exp\left[-k^2\sigma_\alpha^2/2\right]. \tag{5}$$

Inverse Fourier transformation leads to

$$\varphi_\alpha(r) = \frac{Z_\alpha e}{\epsilon' r} \text{erf}(r/\sqrt{2}\sigma_\alpha), \tag{6}$$

where $\text{erf}(x)$ is the error function. In the point particle limit, $\sigma_\alpha \to 0$, $\varphi_\alpha(r)$ reduces to $Z_\alpha e/\epsilon' r$, as expected. For finite σ_α, $\varphi_\alpha(r)$ remains finite as $r \to 0$.

The pair potential between an α-polyion and a β-polyion at a CM-CM distance r is given by

$$v_{\alpha\beta}(r) = \int \varphi_\alpha(r') Z_\beta e \rho_\beta(|\mathbf{r} - \mathbf{r}'|) d\mathbf{r}'. \tag{7}$$

Applying the convolution theorem, the Fourier transform is

$$\hat{v}_{\alpha\beta}(k) = Z_\beta e \hat{\varphi}_\alpha(k) \hat{\rho}_\beta(k) = \frac{4\pi Z_\alpha Z_\beta e^2}{\epsilon' k^2} \exp\left[-k^2\sigma_{\alpha\beta}^2\right], \tag{8}$$

where $\sigma_{\alpha\beta}^2 = (\sigma_\alpha^2 + \sigma_\beta^2)/2$. Inverse Fourier transformation finally yields the set of three pair potentials between identical or opposite polyions

$$v_{\alpha\beta}(r) = \frac{Q_\alpha Q_\beta}{\epsilon' r} \text{erf}(r/2\sigma_{\alpha\beta}). \tag{9}$$

This pair potential remains finite at full overlap, i.e., as $r \to 0$

$$v_{\alpha\beta}(r) \underset{r\to 0}{\sim} u_{\alpha\beta}\left[1 - \frac{r^2}{12\sigma_{\alpha\beta}^2} + \frac{r^4}{160\sigma_{\alpha\beta}^4} - \mathcal{O}(r^6)\right], \tag{10}$$

where the overlap energies are

$$u_{\alpha\beta} = \frac{Q_\alpha Q_\beta}{\sqrt{\pi}\epsilon' \sigma_{\alpha\beta}}. \tag{11}$$

At large distances, $v_{\alpha\beta}(r)$ goes over to the Coulombic pair potential between point ions:

$$v_{\alpha\beta}(r) \underset{r\to\infty}{\sim} \frac{Q_\alpha Q_\beta}{\epsilon' r}\left[1 - \frac{2\sigma_{\alpha\beta}}{\sqrt{\pi} r} e^{-r^2/\sigma_{\alpha\beta}^2}\right]. \tag{12}$$

In order to introduce reduced (dimensionless) physical quantities, we define the following convenient length, energy, and time scales:

$$\text{length scale:} \quad \sigma = \sigma_{+-}, \qquad (13a)$$

$$\text{energy scale:} \quad u = -u_{+-} = \frac{Q_+|Q_-|}{\sqrt{\pi}\epsilon'\sigma_{+-}}, \qquad (13b)$$

$$\text{time scale:} \quad \tau = \left(\frac{m\sigma_{+-}^2}{u}\right)^{1/2}, \qquad (13c)$$

where m is the smaller of the polyanion and polycation masses m_- and m_+. Reduced distances, densities, times, and temperatures are defined as

$$r^* = r/\sigma, \quad n_\alpha^* = n_\alpha\sigma^3, \quad t^* = t/\tau, \quad T^* = k_B T/u,$$

and in the following only reduced units will be used and asterisks are dropped for convenience. Another, related dimensionless parameter is the reduced Bjerrum length for monovalent ions, l_B, which is identical to the Coulomb coupling parameter Γ commonly used in the characterization of strongly coupled plasmas (see, e.g., Ref. [30]):

$$\Gamma = l_B = \frac{e^2}{\epsilon' k_B T \sigma}. \qquad (14)$$

Γ is directly related to the reduced inverse temperature β for a system of polyions by

$$\Gamma = \frac{\sqrt{\pi}}{|Z_+ Z_-|}\beta = \frac{\sqrt{\pi}}{|Z_+ Z_-|}\frac{1}{T}. \qquad (15)$$

Two relevant special cases of the UPM are the following:

(a) The restricted model (URPM) is the symmetric version where polyions are of the same size ($\sigma_+ = \sigma_- = \sigma$) and opposite charge ($Q_+ = -Q_- = Q$). This is the model introduced in our preliminary communication,[29] and most of the results in Secs. III–V will be for the URPM. Note that the set of reduced units introduced above is different from the one we employed in Ref. [29].

(b) A fully asymmetric version of the model (UAPM) consists of polyanions ($Z = |Z_-| \gg 1$) and microscopic cations ($Z_+ = 1$), with $\sigma_- \gg \sigma_+$. This version provides a simple representation of an anionic polyelectrolyte in good solvent and its counterions.

At sufficiently low temperature and density, polyions and polycations of the UPM are expected to cluster into neutral or charged aggregates, as in the case of the PM.[4,27,31,32] In the $T \to 0$ limit, the ground state of the symmetric version (the URPM) is achieved by associating the N polyions into $N/2$ neutral, non-interacting pairs of total energy

$$U_0 = -\frac{N}{2}u. \qquad (16)$$

This energy is finite and extensive so that the URPM is thermodynamically stable according to Ruelle's stability criterion.[33]

Similar considerations are expected to apply to asymmetric versions of the UPM, but the ground-state analysis is much less straightforward, except when $|Z_-|$ is an integer multiple of Z_+ (or conversely). To simplify notations, we consider the case where $Z_+ = 1$ and $|Z_-| = Z$, corresponding to the UAPM. One polyanion and Z counterions may then collapse into a neutral point cluster and the corresponding ground-state energy of N_+/Z neutral clusters would be

$$U_0 = \frac{N_+}{Z}\left[Zv_{+-}(r=0) + \frac{Z(Z-1)}{2}v_{++}(r=0)\right]$$

$$= -N_+ u\left[1 - \frac{Z-1}{Z}\frac{1}{2^{3/2}}(1+\Sigma^2)^{1/2}\right], \qquad (17)$$

where $\Sigma = \sigma_-/\sigma_+ \gg 1$.

For the ground state to be stable, U_0 must be negative. Assuming Z to scale like Σ^3 (volume charge), U_0 is negative provided Z satisfies the inequality

$$Z^2 > \frac{(Z-1)^2}{8}(1 + Z^{2/3}),$$

which requires $Z \lesssim 22$. For larger anion to cation charge ratios the neutral clusters are unstable, and the ground state can no longer be a system of neutral point clusters.

Before presenting the results of our calculations for the UPM in Secs. III–V, two remarks are in order. First, the UPM is a purely Coulombic system and no other force fields are involved. In particular, we do not include the ultrasoft entropic repulsion between interpenetrating coils mentioned in Sec. I. Apart from obvious reasons of simplicity, this is physically justified at low temperatures (where most of the interesting physics will be shown to occur), where Coulombic interactions dominate the effective entropic interactions, which scale like T. Second, a model somewhat similar to the UPM was used previously to investigate a very different Coulombic system, namely, a semi-classical Hydrogen plasma under astrophysical conditions of high temperatures and densities.[34]

III. PAIR STRUCTURE AND THERMODYNAMICS

The local pair structure of the UPM is characterized by the three partial pair distribution functions $g_{++}(r)$, $g_{+-}(r)$, and $g_{--}(r)$; the corresponding pair correlation functions $h_{\alpha\beta}(r) = g_{\alpha\beta}(r) - 1$ go to zero at long distances in the disordered fluid phases. Their Fourier transforms $\hat{h}_{\alpha\beta}(k)$ are related to those of the direct correlation functions $\hat{c}_{\alpha\beta}(k)$ by the set of three coupled Ornstein-Zernike (OZ) relations;[35] solving the latter for the $\hat{h}_{\alpha\beta}(k)$, and introducing the concentrations $x_\alpha = n_\alpha/n$, we find

$$\hat{h}_{++}(k) = \frac{1}{D(k)}[\hat{c}_{++}(k) - x_-\Delta(k)], \qquad (18a)$$

$$\hat{h}_{+-}(k) \equiv \hat{h}_{-+}(k) = \frac{\hat{c}_{+-}(k)}{D(k)}, \qquad (18b)$$

$$\hat{h}_{--}(k) = \frac{1}{D(k)}[\hat{c}_{--}(k) - x_+\Delta(k)], \qquad (18c)$$

where

$$\Delta(k) = \hat{c}_{++}(k)\hat{c}_{--}(k) - \hat{c}_{+-}^2(k),$$

$$D(k) = [1 - x_+\hat{c}_{++}(k)][1 - x_-\hat{c}_{--}(k)] - x_+ x_-\hat{c}_{+-}^2(k),$$

$$(19)$$

and all Fourier transforms are dimensionless, i.e., $\hat{f}(k) = n \int \exp(i\mathbf{k}\mathbf{r}) f(r) d\mathbf{r}$.

The partial structure factors $S_{\alpha\beta}(k)$, which are measurable by x-ray or neutron diffraction experiments, are directly related to the $\hat{h}_{\alpha\beta}(k)$ through[35]

$$S_{\alpha\beta}(k) = \frac{1}{N}\langle \rho_{\mathbf{k}}^{\alpha} \rho_{-\mathbf{k}}^{\beta}\rangle = x_{\alpha}\delta_{\alpha\beta} + x_{\alpha}x_{\beta}\hat{h}_{\alpha\beta}(k), \quad (20)$$

where the Fourier components of the local density operators are

$$\rho_{\mathbf{k}}^{\alpha} = \sum_{i=1}^{N_{\alpha}} \exp(i\mathbf{k} \cdot \mathbf{r}_{i\alpha}). \quad (21)$$

It is convenient to introduce the linear combinations corresponding to total number (N) and charge (C) densities:

$$\rho_{\mathbf{k}}^{N} = \rho_{\mathbf{k}}^{+} + \rho_{\mathbf{k}}^{-}, \quad (22a)$$

$$\rho_{\mathbf{k}}^{C} = Z_{+}\rho_{\mathbf{k}}^{+} + Z_{-}\rho_{\mathbf{k}}^{-}, \quad (22b)$$

and the related structure factors:

$$S_{NN}(k) = \frac{1}{N}\langle \rho_{\mathbf{k}}^{N} \rho_{-\mathbf{k}}^{N}\rangle = \sum_{\alpha}\sum_{\beta} S_{\alpha\beta}(k), \quad (23a)$$

$$S_{NC}(k) = \frac{1}{N}\langle \rho_{\mathbf{k}}^{N} \rho_{-\mathbf{k}}^{C}\rangle = \sum_{\alpha}\sum_{\beta} Z_{\beta} S_{\alpha\beta}(k), \quad (23b)$$

$$S_{CC}(k) = \frac{1}{N}\langle \rho_{\mathbf{k}}^{C} \rho_{-\mathbf{k}}^{C}\rangle = \sum_{\alpha}\sum_{\beta} Z_{\alpha} Z_{\beta} S_{\alpha\beta}(k). \quad (23c)$$

The charge-charge structure factor obeys the Stillinger-Lovett limit, valid for a conducting medium[31]

$$\lim_{k\to 0} \frac{\kappa_{\mathrm{D}}^{2}}{k^{2}} \frac{S_{CC}(k)}{\bar{Z}^{2}} = 1, \quad (24)$$

where $\bar{Z}^{2} = x_{+}Z_{+}^{2} + x_{-}Z_{-}^{2}$ and κ_{D} is the inverse Debye screening length

$$\kappa_{\mathrm{D}}^{2} = \kappa_{\mathrm{D}+}^{2} + \kappa_{\mathrm{D}-}^{2} = 4\pi n_{+}Z_{+}^{2}l_{\mathrm{B}} + 4\pi n_{-}Z_{-}^{2}l_{\mathrm{B}}. \quad (25)$$

Knowledge of the pair structure gives access to a number of thermodynamic properties via standard relations.[35] Using the dimensionless variables defined in Sec. II, the reduced excess internal energy per polyion is given by

$$u^{\mathrm{ex}} = \frac{\beta U^{\mathrm{ex}}}{N}$$

$$= 2\pi n\Gamma \int_{0}^{\infty} \{ x_{+}^{2}Z_{+}^{2}h_{++}(r)\mathrm{erf}(r/2\sigma_{+})$$

$$+ 2x_{+}x_{-}Z_{+}Z_{-}h_{+-}(r)\mathrm{erf}(r/2\sigma_{+-})$$

$$+ x_{-}^{2}Z_{-}^{2}h_{--}(r)\mathrm{erf}(r/2\sigma_{-})\} r\,dr \quad (26a)$$

$$= \frac{\Gamma}{\pi} \int_{0}^{\infty} \{ x_{+}^{2}Z_{+}^{2}\hat{h}_{++}(k)\mathrm{e}^{-k^{2}\sigma_{+}^{2}} + 2x_{+}x_{-}Z_{+}Z_{-}\hat{h}_{+-}(k)\mathrm{e}^{-k^{2}\sigma_{+-}^{2}}$$

$$+ x_{-}^{2}Z_{-}^{2}\hat{h}_{--}(k)\mathrm{e}^{-k^{2}\sigma_{-}^{2}}\} dk, \quad (26b)$$

where the transition from Eq. (26a) to (26b) has been achieved by using Parseval's theorem. The wave numbers k in Eq. (26b)

are dimensionless, i.e., expressed in units of $\sigma^{-1} \equiv \sigma_{+-}^{-1}$.

Similarly, the dimensionless equation of state (with P the pressure) is given by

$$\frac{\beta P}{n} = 1 + \frac{u^{\mathrm{ex}}}{3} - \frac{2\Gamma\sqrt{\pi}}{3}n\int_{0}^{\infty} \left\{ \frac{x_{+}^{2}Z_{+}^{2}}{\sigma_{+}}h_{++}(r)\mathrm{e}^{-r^{2}/4\sigma_{+}^{2}} \right.$$

$$+ \frac{2x_{+}x_{-}Z_{+}Z_{-}}{\sigma_{+-}}h_{+-}(r)\mathrm{e}^{-r^{2}/4\sigma_{+-}^{2}}$$

$$\left. + \frac{x_{-}^{2}Z_{-}^{2}}{\sigma_{-}}h_{--}(r)\mathrm{e}^{-r^{2}/4\sigma_{-}^{2}} \right\} r^{2}dr \quad (27a)$$

$$= 1 + \frac{u^{\mathrm{ex}}}{3} - \frac{2\Gamma}{3\pi}\int_{0}^{\infty} \{ x_{+}^{2}Z_{+}^{2}\sigma_{+}^{2}\hat{h}_{++}(k)\mathrm{e}^{-k^{2}\sigma_{+}^{2}}$$

$$+ 2x_{+}x_{-}Z_{+}Z_{-}\sigma_{+-}^{2}\hat{h}_{+-}(k)\mathrm{e}^{-k^{2}\sigma_{+-}^{2}}$$

$$+ x_{-}^{2}Z_{-}^{2}\sigma_{-}^{2}\hat{h}_{--}(k)\mathrm{e}^{-k^{2}\sigma_{-}^{2}}\} k^{2}dk. \quad (27b)$$

The dimensionless isothermal compressibility χ_{T} is determined by the small k-limit of the number-number structure factor:

$$nk_{\mathrm{B}}T\chi_{\mathrm{T}} = \left(\frac{\partial \beta P}{\partial n}\right)_{\mathrm{T}}^{-1} = \lim_{k\to 0} S_{NN}(k). \quad (28)$$

The entropy S, Helmholtz free energy F, or chemical potentials μ_{+} and μ_{-} cannot be expressed in terms of the pair distribution functions alone. The dimensionless excess Helmholtz free energy per polyion, $f^{\mathrm{ex}} = \beta F^{\mathrm{ex}}/N$, along an isochore can be obtained by standard thermodynamic integration, starting from the high temperature ($\beta = 0$) limit, where $f^{\mathrm{ex}} = 0$, according to

$$f^{\mathrm{ex}}(\beta, n) = \int_{0}^{\beta} u^{\mathrm{ex}}(\beta', n)\frac{d\beta'}{\beta'}. \quad (29)$$

Equivalently, the chemical potentials of the polyions may be calculated by the Kirkwood charging process[36] whereby a test polycation or polyanion is gradually coupled to the N polyions of the system by varying a coupling parameter λ from 0 (non-interacting test particle) to 1 (fully interacting test particle):

$$\mu_{\alpha}^{\mathrm{ex}} = n\int_{0}^{1} d\lambda \int \sum_{\beta} x_{\beta}v_{\alpha\beta}(r)h_{\alpha\beta}(r;\lambda)d\mathbf{r}, \quad (30)$$

where $h_{\alpha\beta}(r;\lambda)$ is the pair correlation function between the test particle of species α and the bath particles of species β corresponding to a pair potential $\lambda v_{\alpha\beta}(r)$.

Because of the absence of strong short-range interactions and the long-range nature of the Coulombic interactions, a "natural" approximation for the pair correlation functions is provided by the random phase approximation (RPA), which is expected to be very accurate at high temperatures ($T \gtrsim 1$) and high densities. The RPA amounts to setting the direct correlation functions equal to their asymptotic limit, for all

inter-particle distances r, namely,

$$c_{\alpha\beta}(r) = -\beta v_{\alpha\beta}(r) = -Z_\alpha Z_\beta \frac{\Gamma}{r} \text{erf}(r/2\sigma_{\alpha\beta}), \quad (31a)$$

$$\hat{c}_{\alpha\beta}(k) = -\beta \hat{v}_{\alpha\beta}(k) = -\frac{4\pi Z_\alpha Z_\beta \Gamma n}{k^2} e^{-k^2\sigma_{\alpha\beta}^2}; \quad \alpha = +, -.$$
$$(31b)$$

Substitution of Eq. (31b) into Eqs. (18a) and (19) leads to simple analytic expressions for the $\hat{h}_{\alpha\beta}(k)$, while Eqs. (23a) and (23c) yield the following explicit expressions for the structure factors:

$$S_{NN}(k) = 1 - \frac{4\pi n l_B}{k^2 D(k)} \Big[x_+^2 Z_+^2 e^{-k^2\sigma_+^2} + x_-^2 Z_-^2 e^{-k^2\sigma_-^2}$$
$$+ 2x_+ x_- Z_+ Z_- e^{-k^2\sigma_{+-}^2} \Big], \quad (32a)$$

$$S_{NC}(k) = -\frac{4\pi n l_B}{k^2 D(k)} \Big[x_+^2 Z_+^3 e^{-k^2\sigma_+^2} + x_-^2 Z_-^3 e^{-k^2\sigma_-^2}$$
$$+ x_+ x_- Z_+ Z_- (Z_+ + Z_-) e^{-k^2\sigma_{+-}^2} \Big], \quad (32b)$$

$$S_{CC}(k) = \bar{Z}^2 - \frac{4\pi n l_B}{k^2 D(k)} \Big[x_+^2 Z_+^4 e^{-k^2\sigma_+^2} + x_-^2 Z_-^4 e^{-k^2\sigma_-^2}$$
$$+ 2x_+ x_- Z_+^2 Z_-^2 e^{-k^2\sigma_{+-}^2} \Big], \quad (32c)$$

where according to Eqs. (19) and (31b)

$$D(k) = 1 + \frac{\kappa_D^2}{\bar{Z}^2 k^2} \Big[x_+ Z_+^2 e^{-k^2\sigma_+^2} + x_- Z_-^2 e^{-k^2\sigma_-^2} \Big]. \quad (33)$$

It is easily verified that $\lim_{k\to 0} S_{NN}(k) = 1$, so that, according to Eq. (28) the isothermal compressibility is that of an ideal gas, a well-known deficiency of the RPA. Similarly, $\lim_{k\to 0} S_{NC}(k) = 0$, so that the RPA predicts that charge and number density fluctuations are decoupled in the long wavelength limit. After some algebra, the charge-charge structure factor (Eq. (32c)) may be cast in the convenient form:

$$\frac{S_{CC}(k)}{\bar{Z}^2} = \frac{\bar{Z}^2 k^2 + x_+ x_- Z_+^2 Z_-^2 \kappa_D^2 [e^{-k^2\sigma_+^2/2} - e^{-k^2\sigma_-^2/2}]}{\bar{Z}^2 k^2 + \kappa_D^2 \left[x_+ Z_+^2 e^{-k^2\sigma_+^2} + x_- Z_-^2 e^{-k^2\sigma_-^2} \right]},$$
$$(34)$$

which clearly satisfies the Stillinger-Lovett condition (Eq. (24)).

In the remainder of this paper, we focus on the symmetric (restricted) version of the UPM, namely, the URPM ($Z_+ = -Z_- = Z$; $n_+ = n_- = n/2$; $\sigma_+ = \sigma_- = \sigma_{+-} \equiv \sigma$). In this case, $v_{++}(r) \equiv v_{--}(r) = -v_{+-}(r)$, and hence $g_{++}(r) \equiv g_{--}(r)$, so that there are only two independent pair distribution functions and structure factors. Furthermore, all the above relations simplify considerably for the URPM. For instance, $S_{NN}(k) \equiv 1$, $S_{NC}(k) \equiv 0$, and $S_{CC}(k)$ reduces to

$$\frac{S_{CC}(k)}{\bar{Z}^2} = \frac{k^2}{k^2 + \kappa_D^2 e^{-k^2\sigma^2}}. \quad (35)$$

For point ions, $S_{CC}(k)$ goes over to the standard Debye-Hückel form. Note that, within RPA, $h_{++}(r) = -h_{+-}(r) = h_{CC}(r)/2$. RPA estimates of the thermodynamic properties are obtained by substituting the above expressions for the pair correlation functions in Eqs. (26b) and (27b). The exact

Kirkwood expression (Eq. (30)) for excess chemical potentials $\mu_+ = \mu_- \equiv \mu$ reduces to

$$\beta\mu^{\text{ex}} = \frac{n}{2} \int_0^1 d\lambda \int \beta v(r) h_{CC}(r; \lambda) d\mathbf{r}$$
$$= \frac{1}{2} \frac{1}{(2\pi)^3} \int_0^1 d\lambda \int \beta\hat{v}(k) \hat{h}_{CC}(k; \lambda) d\mathbf{k}, \quad (36)$$

where $v(r) \equiv v_{++}(r)$, $\beta\hat{v}(k) = \frac{4\pi Z^2 \Gamma}{k^2} e^{-k^2\sigma^2}$, and $h_{CC}(r) = h_{++}(r) - h_{+-}(r)$.

Using the coupled OZ relations for the correlation functions of a test particle partially coupled to the bath particles, one can easily show that

$$\hat{h}_{CC}(k; \lambda) = \frac{\hat{c}_{CC}(k; \lambda)}{1 - \frac{1}{2}\hat{c}_{CC}(k)}, \quad (37)$$

where $\hat{c}_{CC}(k) = \hat{c}_{++}(k) - \hat{c}_{+-}(k) = -2n\beta\hat{v}(k)$ and $\hat{c}_{CC}(k; \lambda) = -2\lambda\beta\hat{v}(k) \equiv \lambda\hat{c}_{CC}(k)$ within RPA. Hence $\hat{h}_{CC}(k; \lambda) = \lambda\hat{h}_{CC}(k)$, so that the integration over λ in Eq. (36) is trivial leading to

$$\beta\mu^{\text{ex}} = \frac{1}{4} \frac{1}{(2\pi)^3} \int \hat{h}_{CC}(k) \beta\hat{v}(k) d\mathbf{k}$$
$$= \frac{\Gamma Z^2}{2\pi} \int_0^\infty \hat{h}_{CC}(k) e^{-k^2\sigma^2} dk \equiv u^{\text{ex}}. \quad (38)$$

The last equality follows from Eq. (26b) adapted to the symmetric case. The result that the excess chemical potential is equal to the excess internal energy per ion is of course only true within RPA.

It is easily verified from Eqs. (35) and (38) that the low temperature limit of the RPA internal energy per ion coincides with the ground-state energy (Eq. (16))

$$\lim_{T\to 0} \frac{U^{\text{RPA}}(T)}{N} = -\frac{N}{2} u = \frac{U_0}{N}. \quad (39)$$

In the high temperature limit, the leading contribution to the reduced excess energy per ion reduces to the Debye-Hückel limiting law for point ions

$$\lim_{T\to\infty} \frac{\beta U^{\text{RPA}}}{N} = -\frac{\kappa_D^3}{8\pi n}. \quad (40)$$

In the zero temperature limit, the pressure is negative

$$\lim_{T\to 0} \frac{P^{\text{RPA}}}{n} = -\frac{u}{12}. \quad (41)$$

Among the standard integral equations for the pair structure, the hypernetted chain (HNC) equation is known to be well adapted for Coulombic fluids.[35] HNC theory supplements the coupled OZ relations linking the total and direct correlation functions $h_{\alpha\beta}(r)$ and $c_{\alpha\beta}(r)$, by the closure relations

$$h_{\alpha\beta}(r) + 1 = g_{\alpha\beta}(r) = \exp\left\{ -\beta v_{\alpha\beta}(r) + h_{\alpha\beta}(r) - c_{\alpha\beta}(r) \right\}$$
$$= \exp\left\{ h_{\alpha\beta}(r) - \Delta c_{\alpha\beta}(r) \right\}, \quad (42)$$

where $\Delta c_{\alpha\beta}(r) = c_{\alpha\beta}(r) + \beta v_{\alpha\beta}(r)$ are the short-range parts of the direct correlation functions, which are expected to vanish rapidly for large r (within the RPA, $\Delta c_{\alpha\beta}(r) \equiv 0$). In the symmetric case, under consideration here, $h_{++}(r)$
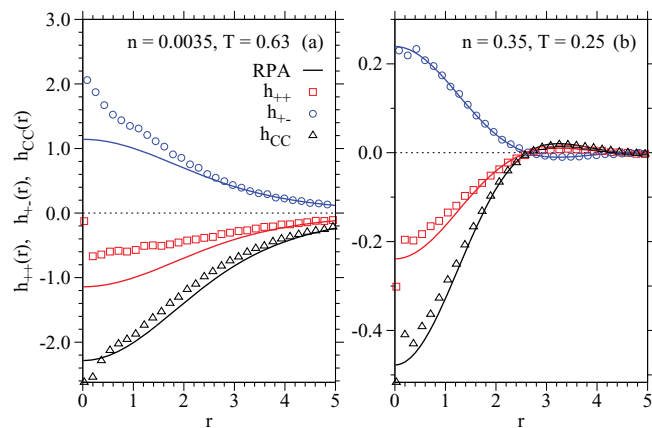
FIG. 1. Total correlation functions $h_{++}(r)$, $h_{+-}(r)$, and $h_{CC}(r)$ from MC simulations (symbols) and RPA (full lines) for two different state points: (a) $n = 0.0035$, $T = 0.63$ and (b) $n = 0.35$, $T = 0.25$.

FIG. 2. Pair distribution functions along the isochore $n = 0.0035$ for three different temperatures (as specified) from MC simulations (symbols) and RPA (full lines): (a) $g_{+-}(r)$ and (b) $g_{++}(r)$.

$\equiv h_{--}(r)$, $c_{++}(r) \equiv c_{--}(r)$, and the three coupled OZ relations reduce to two decoupled equations for the number-number and charge-charge correlation functions $h_{NN}(r) = h_{++}(r) + h_{+-}(r)$, $h_{CC}(r) = h_{++}(r) - h_{+-}(r)$; in k-space the two relations read:

$$\hat{h}_{\alpha\alpha}(k) = \frac{\hat{c}_{\alpha\alpha}(k)}{1 - \frac{1}{2}\hat{c}_{\alpha\alpha}(k)}; \quad \alpha = N, C. \tag{43}$$

HNC theory has the advantage that the excess chemical potential can be calculated from a knowledge of the pair correlation functions alone.[35] The set of Eqs. (42) and (43) is solved numerically by an iterative Picard method, taking particular care of the long-range tails of the direct correlation functions in r- and k-space. Unfortunately, the range of thermodynamic conditions for which the numerical procedure converges is limited to increasingly higher temperatures as the density is reduced. The applicability of the HNC closure is therefore limited to relatively high density and temperatures (see below).

We have compared the RPA and HNC predictions for the pair structure of the URPM to MC results along several isochores. The details of our simulations are described in Appendix A. In the following, we focus on the two isochores $n = 0.0035$ and $n = 0.35$, which are representatives of the system's behavior at low and high density, respectively. Note that we do not investigate here the regime of very low densities, in which special simulation techniques must be employed to ensure ergodicity.[37] Data along the isochores $n = 0.0035$ and $n = 0.35$ are shown in Figs. 1–4, respectively. Figure 1 shows $h_{++}(r)$, $h_{+-}(r)$, and $h_{CC}(r)$ for $n = 0.0035$; $T = 0.63$ and $n = 0.35$; $T = 0.25$. Since these temperatures are below the no-solution line of HNC, we only report the predictions of RPA. At the higher density, RPA is seen to be very accurate for $h_{CC}(r)$, although the RPA symmetry $h_{+-}^{RPA}(r) = -h_{++}^{RPA}(r)$ is broken in the simulation data. The discrepancies between RPA and simulation data are only slightly more pronounced at lower density ($n = 0.0035$, $T = 0.63$), but they increase rapidly as T is lowered due to strong Coulomb correlations (see below).

A comparison between theoretical predictions and MC data at even lower temperatures is made in Fig. 2 along
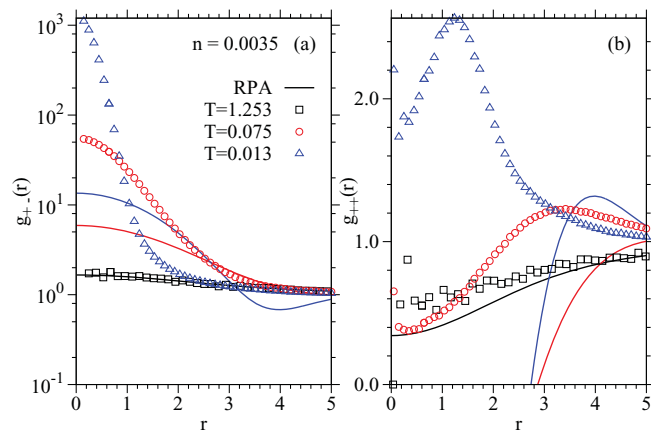
the isochore $n = 0.0035$, and along the isochore $n = 0.35$ in Fig. 3. Strong pairing is evident from inspection of the data for $g_{+-}(r)$ at lower densities and temperatures as expected. Indirect evidence of pairing is also provided by the observation that at the lowest temperatures, along the isochore $n = 0.0035$, $g_{++}(r) > 1$ as $r \rightarrow 0$ despite the Coulomb repulsion between equal sign polyions; this apparent attraction can be rationalized by the formation of tight anion/cation pairs: the anion of a given pair will be preferentially situated between its cationic partner and the cation of another pair, thus favoring the cation-cation approach and the possible formation of trimers and higher order clusters. RPA is unable to properly account for strong ion pairing, both at high and low density. The agreement of HNC predictions with the MC data at high density (see Fig. 3) is good at high temperature but is seen to deteriorate as the temperature is lowered towards the no-solution point (corresponding to $T = 0.044$ at $n = 0.35$). Also note the unphysical predictions of RPA ($g_{++}(r) < 0$) at low density and temperature.

Figure 4(a) shows a comparison between the RPA predictions and MC data for the charge-charge structure factor $S_{CC}(k)$ along the low density isochore $n = 0.0035$. While the
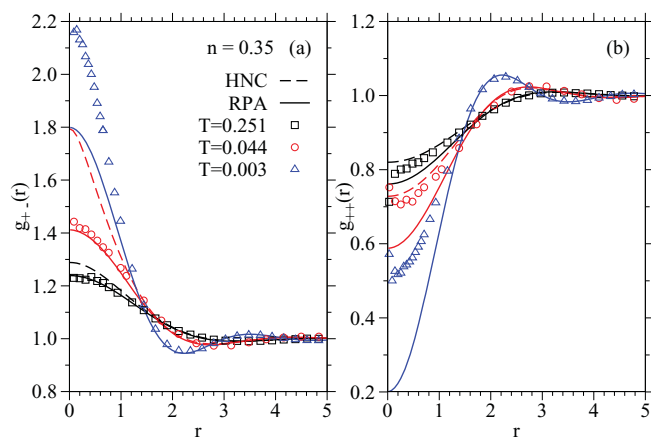

FIG. 3. Pair distribution functions along the isochore $n = 0.35$ for three different temperatures (as specified) from MC simulations (symbols), RPA (full lines), and HNC (dashed lines): (a) $g_{+-}(r)$ and (b) $g_{++}(r)$.
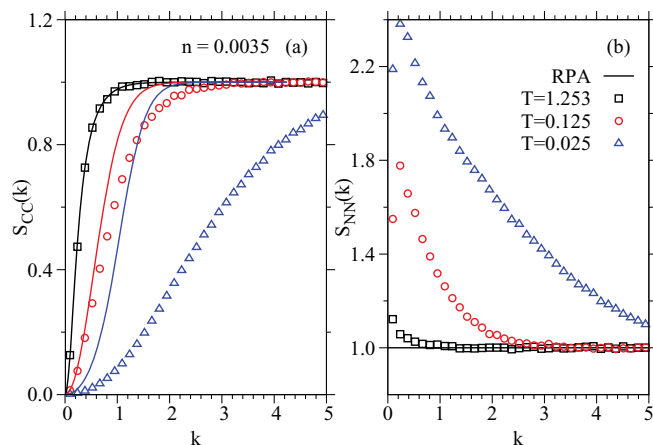
FIG. 4. Structure factors along the isochore $n = 0.0035$ for three different temperatures (as specified) from MC simulations (symbols) and RPA (full lines): (a) $S_{CC}(k)$ and (b) $S_{NN}(k)$.

FIG. 6. Excess internal energy per particle U^{ex}/N as a function of temperature from MC simulations (symbols) and RPA (full lines) along the isochores $n = 0.0035$ (squares) and $n = 0.35$ (circles).

agreement is very good at the higher temperatures ($T \gtrsim 0.2$), it deteriorates rapidly as T is lowered. At the lowest temperatures ($T \lesssim 0.05$), the MC data do not satisfy the Stillinger-Lovett condition (Eq. (24)), while the RPA result (Eq. (34)) obeys the condition by construction. As shown in Ref. 29, a least squares parabolic fit to the low-k MC data [$S_{CC}(k)/Z^2 \simeq k^2/\kappa^2$] yields an effective inverse Debye screening length κ, which is systematically larger than κ_D [defined in Eq. (25)]. The violation of the Stillinger-Lovett limit suggests that the URPM no longer behaves as a purely ionic fluid at low temperatures, due to ion pairing; we will return to this important issue in Sec. IV, where clustering and dielectric response will be analyzed. A similar analysis of $S_{CC}(k)$ along the high density isochore (see Fig. 5) shows excellent agreement between RPA and MC data down to $T = 0.003$, with the effective κ consistently close to κ_D, confirming that the URPM remains ionic throughout: at high densities, anion/cation pairs are short-lived due to the frequent overlap of neighboring pairs.

The results for $S_{NN}(k)$ are shown in Figs. 4(b) and 5(b). The density-density structure factor $S_{NN}(k)$ is seen to increase

rapidly as $k \to 0$ along the isochore $n = 0.0035$, signaling the proximity of a spinodal line as T is lowered. At the spinodal line associated with a phase separation, $S_{NN}(k)$ diverges in the long wavelength limit. Note that, within RPA, $S_{NN}(k) \equiv 1$. The predictions of HNC along the high density isochore indicate a mild increase at small k, consistent with the simulation data. However, the integral equation approach admits no solution in the vicinity of phase coexistence—a well-known defect of the theory. [38,39] All these findings clearly indicate that more sophisticated theoretical tools should be employed to study the low temperature, low density regime of the model.

The RPA, HNC, and MC data for the pair structure may be used to compute the excess internal energy and the equation of state of the URPM via Eqs. (26a) and (26b) and (27a) and (27b), and the isothermal compressibility via Eq. (28). The excess chemical potential follows from Eq. (36), leading to the explicit result (Eq. (38)) within the RPA. Representative comparisons are made for $u^{ex}(n, T) = U^{ex}/N$ in Fig. 6 along the isochores $n = 0.0035$ and $n = 0.35$, and for the total, dimensionless chemical potential $\beta\mu$ in Fig. 7. Simulation results for the density dependence of $\beta\mu$ have been obtained from grand-canonical MC simulations using biased pair insertions. [40] Also included are results for $\beta\mu$ obtained
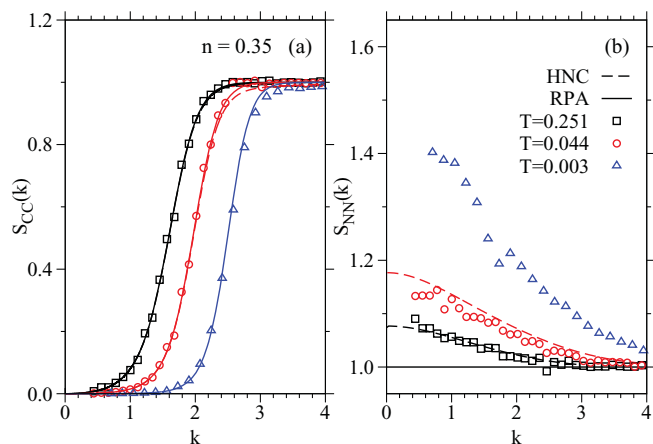

FIG. 5. Structure factors along the isochore $n = 0.35$ for three different temperatures (as specified) from MC simulations (symbols), RPA (full lines), and HNC (dashed lines): (a) $S_{CC}(k)$ and (b) $S_{NN}(k)$.
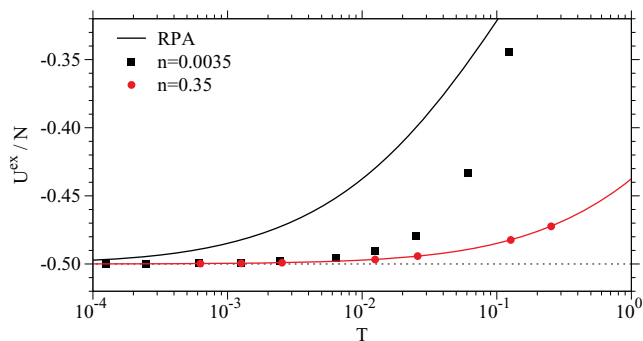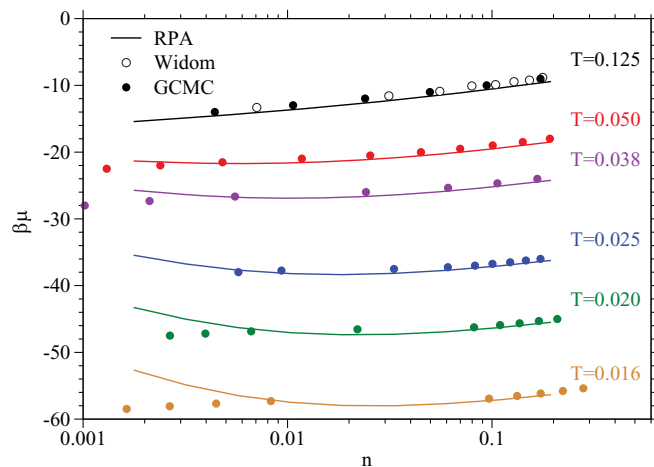

FIG. 7. Dimensionless chemical potential $\beta\mu$ as a function of the density n along several isotherms (as labeled) obtained from the Widom insertion method in NVT MC simulations (open circles), grand canonical MC simulations (full circles), and RPA (full lines).

from standard NVT MC simulations using the Widom insertion method.[41] The agreement between RPA and simulation results is good only at sufficiently high temperature and density. We note that for these temperatures and densities, RPA- and HNC-data agree within symbol size. For completeness, we note that the Helmholtz excess free energy per ion can finally be obtained from the thermodynamic relation

$$f^{ex} = \frac{\beta F^{ex}}{N} = \beta\mu^{ex} - \frac{\beta P^{ex}}{n} . \tag{44}$$

IV. CLUSTERING AND DIELECTRIC RESPONSE

The structural data and thermodynamic properties reported in Sec. III point to strong clustering of anions and cations at low temperatures and densities. Pairing of oppositely charged ions, as well as the formation of larger aggregates are well documented for the RPM,[4,27,28,31,32] where clusters carry large multipole moments (dipoles in the case of pairs) due to the ionic cores, which induce charge separation. In the case of the URPM opposite charges can overlap, so that clusters do not carry permanent multipoles, but are polarizable entities. Their mutual interactions are thus expected to be much weaker than in the case of the RPM.

Clusters can be properly defined only at sufficiently low densities, and even then there is always some arbitrariness in their definition. We have used a standard geometric definition of m-clusters, namely that m ions form an m-mer if each ion lies within a given distance r_c of at least one other ion in the cluster. The cut-off r_c is taken to be typically close to 1.0 (in units of σ), corresponding to a situation, where the charge distributions of polyions touch (cf. Eq. (2)), and we have examined the sensitivity of the cluster analysis to variations of r_c. We have thus determined the cluster distribution functions, i.e., the fractions $P(m)$ of m-mers, averaged over all configurations generated in MC and MD simulations. Typical examples of the resulting histograms are shown in Fig. 8 for $n = 0.0035$ and two temperatures. At the higher temperature ($T = 0.125$), monomers (i.e., free ions) are by far the majority species, and $P(m)$ is seen to decrease monotonically and rapidly as m increases. At the lower tempera-
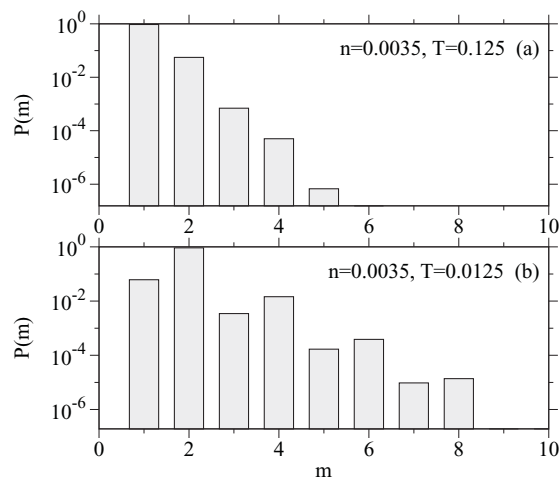
FIG. 8. Cluster distribution function $P(m)$ for (a) $T = 0.125$ and (b) $T = 0.0125$ along the isochore $n = 0.0035$.
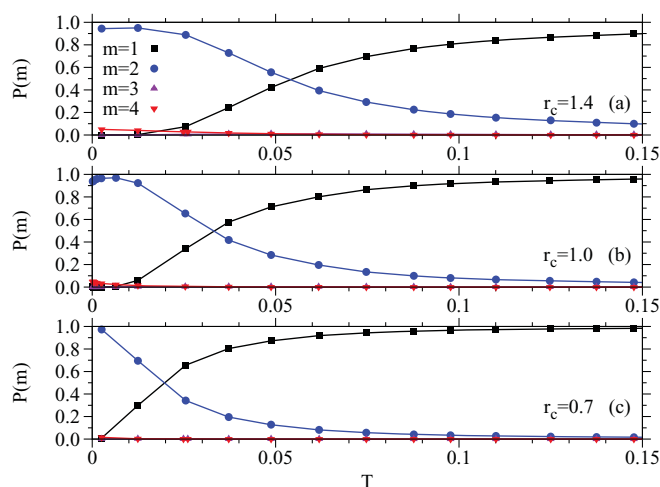
FIG. 9. Fractions of selected cluster types $P(m)$ as functions of temperature along the isochore $n = 0.0035$: $P(m = 1)$ (squares), $P(m = 2)$ (circles), $P(m = 3)$ (triangles), and $P(m = 4)$ (reversed triangles). The three panels show results obtained using the following values of the cut-off r_c: (a) $r_c = 1.4$, (b) $r_c = 1.0$, and (c) $r_c = 0.7$.

ture ($T = 0.0035$), pairs constitute the most common m-mers (with a fraction $P(2)$ very close to 1), and the variation with m is alternating, with neutral m-mers (pairs, tetramers, etc.) being much more probable than charged m-mers (corresponding to odd values of m).

The variation of $P(m)$ as a function of temperature, for $1 \leq m \leq 4$, is illustrated in Fig. 9 for three different choices of the cut-off r_c. Although there are significant quantitative differences between the three sets of data, the trends are the same. As expected, the fraction $P(1)$ of monomers is vanishingly small at the lowest temperatures; it increases rapidly towards 1 for $T \gtrsim 0.05$. Simultaneously the fraction $P(2)$ of dimers drops dramatically as T increases; the fraction $P(3)$ of trimers is negligibly small throughout, while the fraction of tetramers is non-negligible at the lowest temperatures. These trends agree with intuitive expectation, but our analysis provides a quantitative estimate of the temperature range associated with the onset of pairing. The onset of pairing along the isochore $n = 0.0035$ is seen to be rapid, but continuous. A similar cluster analysis carried out along several low density isochores shows that the temperature at which $P(m = 2) \simeq P(m = 1) \simeq 0.5$ drops as the density n increases.

Using MD simulations, we have estimated the mean cluster lifetimes τ_m for m-mers with $1 \leq m \leq 4$ as functions of temperature, along the isochore $n = 0.0035$. The lifetime is defined as the minimum time span during which a cluster is formed by exactly the same set of particles, and is thus bounded from below by the typical collision time between clusters. Results are shown in Fig. 10. The monomer lifetime is seen to increase from $\tau_1 \simeq 2$ up to $\tau_1 \simeq 15$ as the temperature rises, while the opposite trend of the dimer lifetime is seen to be much faster, with $\tau_2 = 10^3$ at the lowest T, dropping rapidly to $\tau_2 \simeq 5$ at $T \simeq 0.05$, the temperature at which τ_1 and τ_2 cross. The lifetimes τ_3 and τ_4 of trimers and tetramers are even smaller at high T, although they tend to increase in the low-temperature, paired regime.
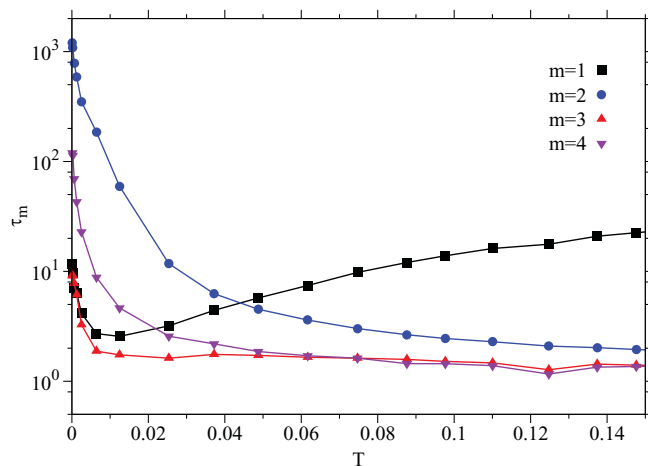
FIG. 10. Cluster lifetime τ_m at $n = 0.0035$ as a function of temperature for selected cluster types: $m = 1$ (squares), $m = 2$ (circles), $m = 3$ (triangles), and $m = 4$ (reversed triangles).

FIG. 12. Dimensionless, effective dimer-dimer potential $\beta v_{2,2}(r)$ for $n = 0.0035$, $T = 0.025$. Inset: Effective potentials on a double-logarithmic scale. The dashed line indicates the asymptotic behavior expected at large r (see Appendix B).

At the lower temperatures, where the lifetimes τ_2 of pairs are long, it makes sense to consider the systems as made up of three "species," namely, free polyanions, polycations, and neutral polyanion-polycation pairs ("chemical picture"). Under those conditions, one may determine monomer-dimer and dimer-dimer distribution functions $g_{1,2}(r)$ and $g_{2,2}(r)$ between isolated monomers and dimers that are not part of larger clusters, in MC or MD simulations. Examples are compared to the monomer-monomer pair distribution function $g_{1,1}(r)$ in Fig. 11, for $n = 0.0035$ and $T = 0.025$, i.e., close to the pairing transition. $g_{1,1}(r)$ is dominated by the strong anion-cation attraction, leading to a pronounced peak at $r = 1$. $g_{1,2}(r)$ and $g_{2,2}(r)$ are seen to exhibit modest peaks at slightly larger distances pointing to rather weak correlations. Note that all three pair distribution functions vanish for $r \lesssim r_c = 1.0$ by construction, because for shorter CM-CM distances the two monomers would be identified as a single dimer, a monomer and a dimer would be identified as a single trimer, and two
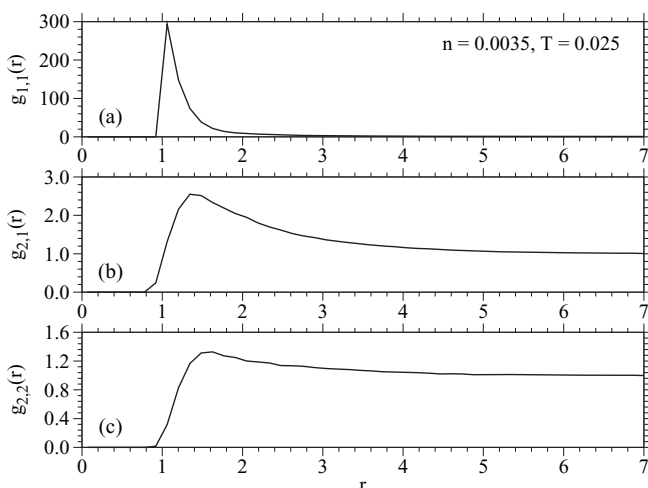
dimers would be identified as a single tetramer, implying an apparent infinite barrier.[31]

In view of the low density, the pair distribution function data may be inverted to determine effective monomer-monomer and monomer-dimer pair potentials, $v_{1,2}(r)$ and $v_{2,2}(r)$, by a simple Boltzmann inversion

$$v_{n,m}(r) = -k_B T \ln g_{n,m}(r). \tag{45}$$

The resulting effective potentials are pictured in Figs. 12 and 13. As explained above, the short-range repulsion is an artifact linked to cluster identity. Beyond $r = r_c$ the monomer-dimer and dimer-dimer potentials are seen to be weak and attractive. In view of the statistical uncertainties, the asymptotic behaviors at large distances, illustrated by the insets in Figs. 12 and 13, are in reasonable agreement with the theoretical predictions $v_{1,2}(r) \sim 1/r^4$ and $v_{2,2}(r) \sim 1/r^6$ for isolated monomer-dimer and dimer-dimer pairs (see Appendix B). These are of course the same asymptotic behaviors as for

FIG. 11. Distribution functions $g_{m,n}(r)$ between the centers of mass of selected cluster types for $n = 0.0035$, $T = 0.025$: (a) monomer-monomer $g_{1,1}(r)$, (b) monomer-dimer $g_{1,2}(r)$, and (c) dimer-dimer $g_{2,2}(r)$.
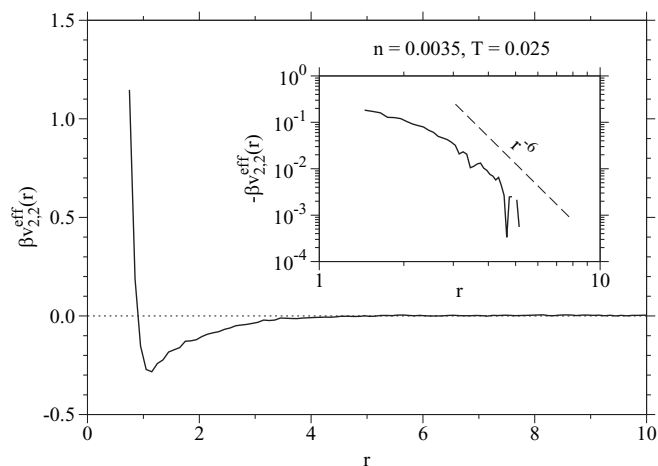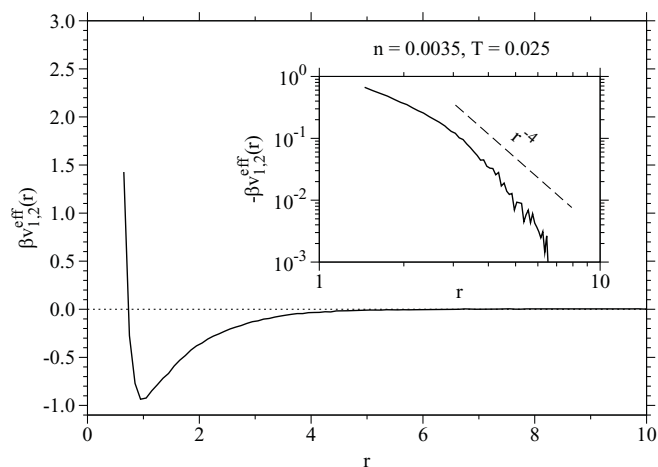

FIG. 13. Dimensionless, effective monomer-dimer potential $\beta v_{1,2}(r)$ for $n = 0.0035$, $T = 0.025$. Inset: Effective potentials on a double-logarithmic scale. The dashed line indicates the asymptotic behavior expected at large r (see Appendix B).

van der Waals-London dispersion interactions between polarizable atoms or molecules, but the prefactors are proportional to k_BT in the present, purely classical case, while they are independent of temperature in the atomic case, since they result from quantum averages over the electronic ground state.

Another diagnostic for clustering is provided by the dielectric response of the URPM. We have shown in Sec. III that at high temperatures and densities, the system behaves as a conductor, obeying the Stillinger-Lovett perfect screening condition (Eq. (24)). However, as illustrated in Fig. 4, the Stillinger-Lovett condition is violated at low densities and temperatures pointing to a dielectric, rather than conducting behavior. According to static linear response theory,[35] the charge-charge structure factor is related to the k-dependent dielectric response function by

$$\frac{1}{\epsilon(k)} = 1 - \frac{\kappa_D^2}{k^2} \frac{S_{CC}(k)}{\bar{Z}^2}. \qquad (46)$$

Taking the $k \to 0$ limit, where $S_{CC}(k) \simeq \bar{Z}^2 k^2 / \kappa^2$, we arrive at the following expression for the macroscopic dielectric permittivity ϵ:

$$\frac{1}{\epsilon} = \lim_{k \to 0} \frac{1}{\epsilon(k)} = 1 - \frac{\kappa_D^2}{\kappa^2}. \qquad (47)$$

In a conducting medium, $\kappa \equiv \kappa_D$ and $\epsilon \to \infty$ as expected. At sufficiently low T and n, all polyions are paired and the MC data show that $\kappa > \kappa_D$, so that ϵ takes on a finite value characteristic of an insulating, dielectric medium

$$\infty > \epsilon = \frac{1}{1 - \kappa_D^2 / \kappa^2} > 1. \qquad (48)$$

Equivalently, ϵ may be estimated form Kirkwood's fluctuation formula[42] adapted to simulations carried out under metallic boundary conditions:[43]

$$\epsilon = 1 + \frac{4\pi}{3k_BT} \frac{\langle |\mathbf{M}|^2 \rangle - |\langle \mathbf{M} \rangle|^2}{V}, \qquad (49)$$

where $\mathbf{M} = \sum_i Q_i \mathbf{r}_i$ is the total dipole moment of the system.

From the permittivities estimated using Eq. (49), it is possible to calculate a "dielectric order parameter," defined as $(\epsilon - 1)/\epsilon$, which equals 1 in the conducting phase and is close to 0 in the insulating phase. The values of $(\epsilon - 1)/\epsilon$ obtained from MC simulations along the isochore $n = 0.0035$ are shown in Fig. 14 together with the corresponding percentage of monomers $P(m = 1)$. The dielectric order parameter signals a sharp transition around $T \approx 0.04$, which correlates with the rapid increase of the fraction of free ions. In the inset of Fig. 14, we can see that ϵ remains nearly constant up to $T \simeq 0.025$, beyond which ϵ increases sharply towards a high temperature limit close to $\epsilon \simeq 10^3$ (cf. Ref. 29), typical of a finite conducting medium (for an infinite conductor, $\epsilon \to \infty$). The correlation between $(\epsilon - 1)/\epsilon$ and $P(m = 1)$ is striking and validates the picture of a transition from a low temperature dielectric (insulator) state to a high temperature ionic (conductor) state driven by the break up of ion pairs. The "conductor-insulator" transition is seen to be fast, but continuous, which may well be a finite size effect. Simulations on larger systems and a finite size scaling analysis will be re-
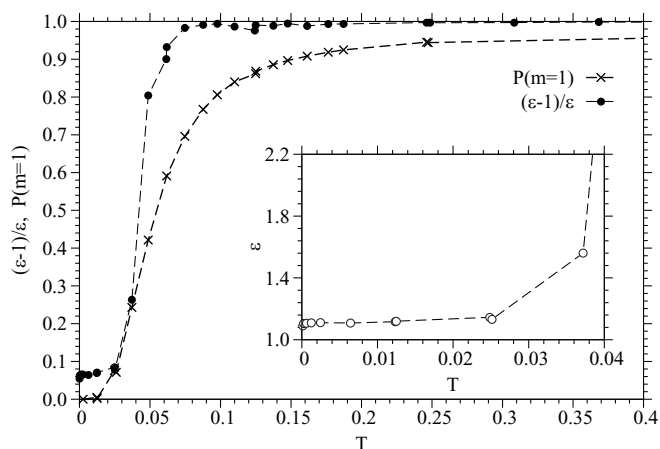

FIG. 14. Dielectric order parameter $(\epsilon - 1)/\epsilon$ (filled circles) obtained from Eq. (49) and fraction of free ions $P(m = 1)$ (crosses) at $n = 0.0035$ as functions of temperature. Inset: enlarged view of the low-temperature behavior of ϵ.

quired to find out if the transition becomes discontinuous in the thermodynamic limit.

The above analysis has been repeated along several low density isochores, and the locus of points in the (n, T) plane, where $P(m = 1) = 0.5$, yields an estimate of pairing (or CI) transition line, which is shown in Fig. 18. In the portion of the phase diagram studied herein, the transition is seen to take place at lower temperatures as the density increases, contrary to what could be expected from a simple "chemical equilibrium" picture[27] and to what is found in the RPM.[28]

V. POLYION DYNAMICS

Time-dependent correlation functions are readily calculated by MD simulations, and provide a quantitative characterization of single-particle and collective ion dynamics as well as giving access to linear transport coefficients, such as ion mobility and electrical conductivity. The latter provides an unambiguous diagnostic of a CI transition. We note that Brownian dynamics simulations would be more appropriate for the system at hand, since they account for solvent effects. However, since we are interested in qualitative, rather than quantitative aspects of the dynamics, we prefer to employ here the more efficient MD simulations, which are capable of exploring longer time windows.

Let $\mathbf{r}(t)$ and $\mathbf{v}(t)$ denote the position and the velocity of any given polyion at time t; the normalized velocity autocorrelation functions of the anions and cations are identical for the symmetric URPM and defined by

$$Z_+(t) = Z_-(t) = Z(t) = \frac{\langle \mathbf{v}(t) \cdot \mathbf{v}(0) \rangle}{\langle v^2 \rangle}, \qquad (50)$$

where $\mathbf{v}(0)$ denotes the initial velocity, $\langle v^2 \rangle = 3k_BT/m$, and statistical averages are taken along the trajectories of individual ions, and over all N ions. Examples of MD-generated correlation functions $Z(t)$, for $n = 0.0035$ and several temperatures, are shown in Fig. 15. At the higher temperatures, $Z(t)$ is seen to decay essentially exponentially. However, the relaxation time of $Z(t)$ increases with increasing T. This
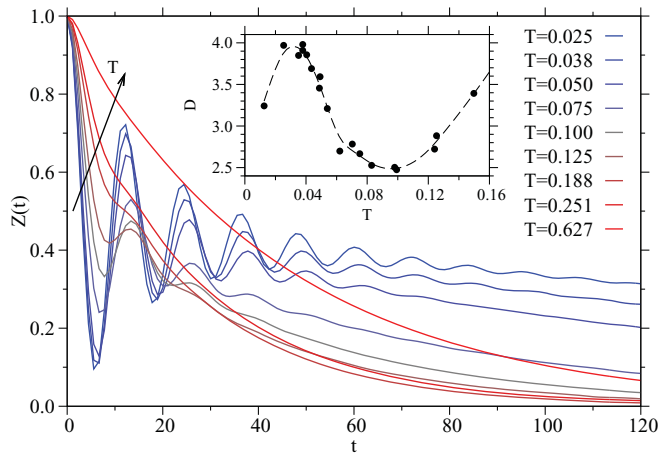
FIG. 15. Velocity auto-correlation function $Z(t)$, as defined in Eq. (50), at $n = 0.0035$ for different temperatures (as labeled). Inset: self diffusion constant D evaluated via Eq. (52) as a function of temperature.
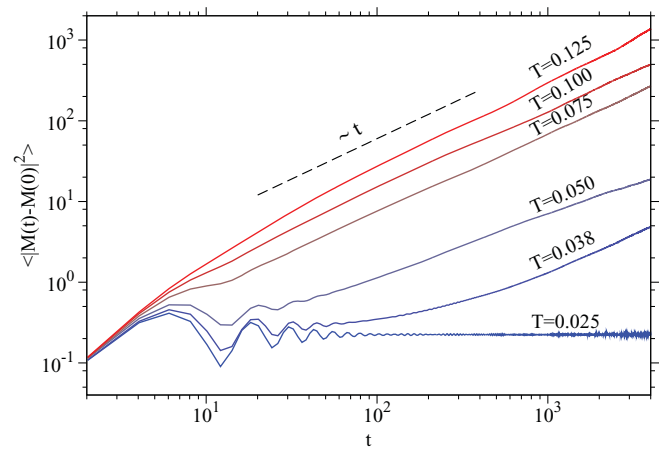

FIG. 16. Mean square displacement $\langle |\mathbf{M}(t) - \mathbf{M}(0)|^2 \rangle$ of the total electric dipole $\mathbf{M}(t)$ as a function of time at $n = 0.0035$ for several temperatures (as labeled). The dashed line indicates the asymptotic behavior expected for a conducting system.

counter-intuitive result can be explained in terms of the ultrasoft nature of the potential: at higher T, collisions become less and less effective in decorrelating the ion velocities, since particles barely feel each other's influence. Thus, the "effective" collision time increases with increasing T. The relaxation changes dramatically at the lower temperatures, where $Z(t)$ decays much more slowly after an initially strong oscillatory regime. This striking behavior may be rationalized in terms of anion-cation pair formation. The oscillations correspond to the vibrations of the ions relative to the CM of a "bound" pair. The measured reduced angular frequency, $\omega \simeq 0.6$ is close to the frequency of the relative motion of two oppositely charged ions within the harmonic potential (see Eq. (10))

$$v_{+-}(r) = -u + u \frac{r^2}{12\sigma^2}, \qquad (51)$$

i.e., $\omega_{+-} = \sqrt{1/3} \simeq 0.58$, independent of temperature. The slow decay of $Z(t)$ at long times may be associated with the motion of the long-lived pair within which the ion is bound. Due to the weakness of the interaction between pairs (cf. Fig. 12), the motion of neutral pairs is nearly ballistic, resulting in the very slow relaxation shown in Fig. 15. The self-diffusion constant of the ions, $D_+ = D_- = D$ may be calculated by integrating the velocity auto-correlation function (Eq. (50)),[35] or, more accurately, from the asymptotic slope of the mean square displacement of an ion from its initial position, according to Einstein's relation:[35]

$$D = \lim_{t \to \infty} \frac{\langle |\mathbf{r}(t) - \mathbf{r}(0)|^2 \rangle}{6t}. \qquad (52)$$

The corresponding ion mobility is $\mu = D/k_B T$.

The variation of D with temperature is shown in the inset of Fig. 15. D is seen to first drop as T decreases, which is the usual behavior observed in "normal" liquids before increasing sharply for $T < 0.08$ and go through a pronounced maximum around $T \simeq 0.03$ below which D decreases again towards zero. This unusual non-monotonic behavior is obviously a direct consequence of pairing: as argued earlier, pairing leads to a system of nearly non-interacting entities which move almost freely, thus explaining the sharp rise in mobility.

Once pairing is complete and no free ions are left, the diffusion constant will drop again with temperature.

We now turn to the electrical conductivity σ_e per unit volume of the URPM. σ_e is determined by the asymptotic slope of the mean square displacement of the total electric dipole $\mathbf{M}$, according to the generalized Einstein relation,

$$\sigma_e = \frac{1}{V k_B T} \lim_{t \to \infty} \frac{\langle |\mathbf{M}(t) - \mathbf{M}(0)|^2 \rangle}{6t}, \qquad (53)$$

which is equivalent to the familiar Green-Kubo relation linking σ_e to the electric current autocorrelation function;[35] in view of the large statistical uncertainties of the latter, as generated in MD simulations, the Einstein relation (Eq. (53)) is preferable to estimate σ_e. Data for the diffusion $c(t) = \langle |\mathbf{M}(t) - \mathbf{M}(0)|^2 \rangle$ of the total dipole along the isochore $n = 0.0035$ are shown in Fig. 16. Note that ions must be allowed to leak out of the periodically repeated simulations cell when calculating $\mathbf{M}(t)$, to allow for diffusion in an unbounded volume. The long-time slopes of the $c(t)$-curves yield σ_e.
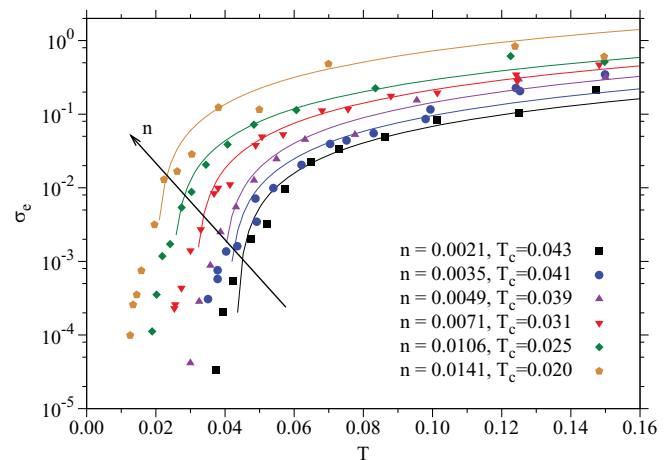

FIG. 17. Electrical conductivity σ_e, evaluated via Eq. (53), as a function of temperature along different isochores (as labeled). T_c indicates the estimated temperature where σ_e vanishes, according to power-law fits $\sigma_e \sim (T - T_c)^\nu$ with $\nu = 1.2$ (full lines). The estimated uncertainty on ν is ± 0.02.
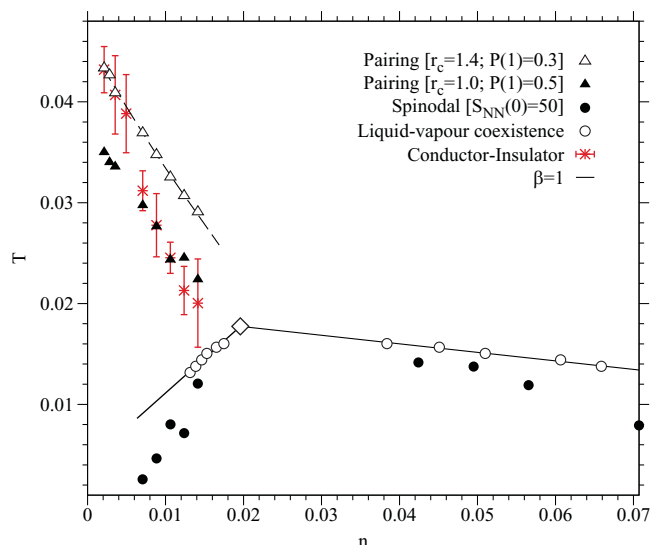
FIG. 18. Current estimate of the phase diagram of the URPM in the (T, n)-plane. Empty circles: coexistence points obtained via GCMC simulations (from Ref. 29). Full line: fit to the coexistence line, assuming a critical exponent $\beta = 1$. Rotated empty square: Estimate of the critical point assuming a critical exponent $\beta = 1$. Filled circles: Spinodal line estimated from the condition $S_{NN}(k = 0) \approx 50$. Open triangles: Pairing transition points estimated from the condition $P(m = 1) = 0.3$ with $r_c = 1.4$ (as in Ref. 29). Filled triangles: Pairing transition points estimated from the condition $P(m = 1) \approx P(m = 2) = 0.5$ with $r_c = 1.0$. Stars: CI transition points estimated from the vanishing of the electrical conductivity (see text for definition).

Figure 16 shows that the asymptotic linear regime is rapidly reached at the higher temperatures, while at the lower temperatures the regime is only reached after reduced times $t \gtrsim 10^3$. At the lowest temperature investigated, $c(t)$ appears to tend to a constant, i.e., its slope and hence σ_e, are zero, corresponding to an insulating state. Note that $c(t)$ exhibits oscillations at the lower temperatures reminiscent of those observed in $Z(t)$ (cf. Fig. 15), of comparable frequency, which are once again ascribable to pairing. We have repeated the electrical conductivity analysis along several low density isochores. The data for the temperature dependence of σ_e are shown in Fig. 17. The conductivity is seen to drop to zero at increasingly low temperatures as the density increases. Assuming a power-law dependence $\sigma_e \sim (T - T_c)^\nu$ with a fixed value of $\nu \simeq 1.2$, least squares fits provide a set of "critical" temperatures T_c at which $\sigma_e(T)$ appear to vanish (indicated by the labels in Fig. 17). These results provide an estimate of a CI transition line in the (n, T) plane. This line is compared in Fig. 18 to the pairing transition line which provides another estimate of the location of the CI transition. The two lines are seen to be roughly parallel and reasonably close. We also include in Fig. 18 the pairing transition line reported in Ref. 29, in which different values of r_c and of the "critical" fraction of free ions $P(m = 1)$ were used. As suggested by Fig. 14, different choices of $P(m = 1)$ would correspond to different values of a "critical" dielectric permittivity ϵ.

VI. DISCUSSION AND CONCLUSIONS

We have introduced a model of interpenetrating polyanions and polycations, carrying extended, continuous charge distributions. We expect this ultrasoft primitive model to be relevant for the study of the aggregation of oppositely charged polyelectrolytes in good solvent. Most of the results presented in this paper are restricted to the symmetric version of the model, the URPM. Interactions between polyions are purely Coulombic; in particular, contrary to the familiar restricted primitive model of electrolytes, no hard cores are involved. We have reported extensive simulation results and theoretical predictions characterizing the pair structure, clustering, thermodynamic, and dynamical properties of the URPM over a wide range of temperatures and densities. Concerning the static (structural and thermodynamic) properties, the RPA proves to be a quantitatively reliable approximation at high densities, corresponding to the fully ionic, conducting regime. At low temperature and density, however, the RPA and even the HNC theory fail completely, due to the formation of long-lived anion/cation pairs and some larger, mostly neutral clusters.

The low density, low temperature data for pairing dielectric permittivity ϵ and electrical conductivity σ_e provide strong evidence of a transition between an insulating phase, characterized by finite values of ϵ and a vanishing σ_e (signaling a vanishing concentration of unpaired ions), and a fully ionic, conducting state at higher n and T, where σ_e takes on non-zero values and ϵ is very large. Further, indirect evidence for a CI transition is provided by the unusual variation of the polyion mobility with temperature at low density.

At sufficiently low T the CI transition gives way to a first order phase separation between a low density insulating phase and a high density conducting phase. The analysis of simulation data for relatively small system sizes provides some preliminary evidence for the existence of an upper tricritical point terminating the phase coexistence line near the junction with the CI line.[29] The exact nature of the CI transition above the putative tricritical point is not entirely clear. The simulation results presented herein and in Ref. 29 point to a continuous transition, possibly broadened by finite size effects. The tentative phase diagram seems to differ qualitatively from that of the RPM, where criticality belongs almost certainly to the Ising universality class,[44,45] and there is no strong evidence for a CI line above T_c. The qualitatively different behaviors of the hard core and penetrable electrolytes are most probably linked to the very different nature of the anion/cation pairs which dominate the insulating phase: they are weakly interacting, polarizable entities in the case of the URPM, while they are strongly interacting dipolar "molecules" in the RPM.[46] Interestingly, the phase diagram of the URPM is more reminiscent of that of the two-dimensional Coulomb gas involving logarithmic interactions between ions (oppositely charged hard disks). In the low density limit, this model is known to undergo an infinite order, Kosterlitz-Thouless (KT) (Ref. 47) transition between a dielectric phase of bound ion pairs and a conducting phase of free ions. In the zero density limit, the KT transition is characterized by a discontinuous jump of the dielectric permittivity from a finite value to infinity as the transition temperature is approached from below. MC simulations on finite systems show that the KT (or CI) transition is continuous (rounded), and that the transition temperature drops

with increasing density; the CI line terminates close to the critical point of a first order vapor-liquid coexistence curve.[48,49] Within statistical uncertainties, the simulations show some evidence of a cusp at the top of the vapor-liquid coexistence curve, suggesting a tricritical point (rather than the regular critical point observed in the three-dimensional equivalent of the Coulomb gas, namely, the RPM). These findings are confirmed by mean field calculations within the chemical representation of a mixture of free ions and bound (Bjerrum) pairs.[50]

In order to confirm a similar scenario in the three-dimensional URPM, it will be crucial to investigate finite size effects within a full finite size scaling analysis, requiring extensive further simulations for several system sizes (for a pedagogical review of finite size scaling techniques, see Ref. 51). The natural order parameters for such an analysis are Δn, i.e., the difference in density of the two coexisting phases, and the fluctuation of the total dipole moment per unit volume, which is intimately related to the dielectric permittivity (see Eq. (49)); such an investigation is under way and will be the main object of a forthcoming publication.

Future developments of our work include an extension of the URPM to non-symmetric versions of the UPM, which will involve less straightforward aggregation patterns, and the generalization of the model to oppositely charged polyions in the presence of microscopic co- and counterions (e.g., from added salt) which will lead to screened effective interactions between the polyions as opposed to the bare Coulombic interactions considered in the present work. The objective of this generalization will be to investigate the influence of screening by microions on the CI transition and phase separation.

APPENDIX A: SIMULATION METHODS

Numerical simulations of the URPM have been performed for systems composed of $N = 1000$ polyions in a cubic cell with periodic boundary conditions using the Ewald summation scheme to account for the long range of the interactions. In the following, we briefly summarize the key equations and the parameters employed in our simulations. Following a standard procedure,[52] we introduce screening charge distributions of shape

$$\rho'_\alpha(\mathbf{r}) = \left(\frac{1}{2\pi\sigma'} \right)^{3/2} \exp\left[-\frac{r^2}{2\sigma'^2} \right], \tag{A1}$$

such that the screening charge distribution around a particle of species α is $-Z_\alpha \rho'(\mathbf{r} - \mathbf{r}_i)$ [cf. Eq. (2)]. Note that, in general, the width σ' of the screening distribution need not coincide with the one of the actual Gaussian distribution. Using the standard Ewald summation scheme, the total interaction energy U can then be expressed as

$$U = U_k + U_r - U_s, \tag{A2}$$

where U_k and U_r are the Fourier and real space contributions, respectively, and U_s is a self-term correcting for the interaction between the screening distribution and its equal and opposite compensating distribution. For the URPM, the three terms read

$$U_k = \frac{1}{2V} \sum_{\{\mathbf{k}\}} \frac{4\pi}{k^2} \exp\left[-\frac{k^2\tilde{\sigma}^2}{2} \right] |\rho_\mathbf{k}|^2, \tag{A3}$$

$$U_r = \frac{1}{2} \sum_{i=1}^{N} \sum_{i=1}^{N'} \frac{Z_i Z_j}{\epsilon} \left[\frac{\mathrm{erf}(r/2\sigma)}{r} - \frac{\mathrm{erf}(r/\sqrt{2}\tilde{\sigma})}{r} \right], \tag{A4}$$

$$U_s = \frac{1}{\sqrt{2\pi}\tilde{\sigma}} \sum_{i=1}^{N} Z_i^2, \tag{A5}$$

where $\rho_\mathbf{k} = \sum_i Z_i \exp(i\mathbf{k} \cdot \mathbf{r}_i)$ and we have introduced the notation $\tilde{\sigma} = \sqrt{\sigma^2 + \sigma'^2}$. Note that the familiar expression for U_k in the case of purely Coulombic interaction is recovered by substituting $\tilde{\sigma} \to \sigma$ in Eq. (A3). Expressions for the forces between charge distributions (needed in MD simulations) are derived in a similar manner.

When $\sigma' = \sigma$, the real space contribution is identically zero and the calculation of the potential energy and the forces can be carried out entirely in Fourier space. Note that this is possible only because the effective potential $v_{\alpha\beta}(r)$ [see Eq. (9)] is bounded. The sum in Eq. (A3) is carried out for all wave vectors $\mathbf{k}$ such that $|\mathbf{k}|$ is smaller than some cut-off value k_c. The error in the evaluation of U_k can then be roughly estimated as[53]

$$\varepsilon = \frac{1}{\epsilon} \frac{\exp\left(-k_c^2\sigma^2\right)}{k_c^2}. \tag{A6}$$

In our simulations, we used indeed $\sigma' = \sigma$ and adjusted k_c so as to keep the nominal error ε constant at 10^{-3}. As a consequence, the actual number N_k of wave vectors used for the evaluation of U_k varied as a function of the density (as $N_k \sim V^{-1/3}$), ranging from 2.5×10^2 at $n = 0.35$ to 4.2×10^4 at $n = 0.0035$. We found that the chosen value of ε was sufficient to converge structural and dynamic properties below the noise level. To illustrate this, in Fig. 19 we compare results for the structure factors $S_{NN}(k)$ and $S_{CC}(k)$ at $n = 0.0035$ obtained using $\varepsilon = 10^{-2}$, 10^{-3}, and 10^{-4}. We note that the effect of reducing ε becomes slightly more pronounced at low T. We remark that these small discrepancies are, however, irrelevant for the purposes of this work.

At even lower densities ($n \lesssim 0.001$), the number of wave vectors required to keep ε constant becomes too large for an efficient computation of Eq. (A3). In this regime, a simple decimation strategy could be used to reduce the number of wave vectors in each spherical shell $k \pm \delta k$. Alternatively, one could use screening charge distributions with width $\sigma' \neq \sigma$, so as to move part of the computational effort into real space. In practice, however, we hardly obtained any benefit from using an optimized σ', at least in the range of state parameters investigated in the current study. In must be noted, in fact, that the range of the pair potential entering Eq. (A4) is relatively long compared to the complementary error function, normally encountered for pure Coulombic interactions. As

244514-14   Coslovich, Hansen, and Kahl

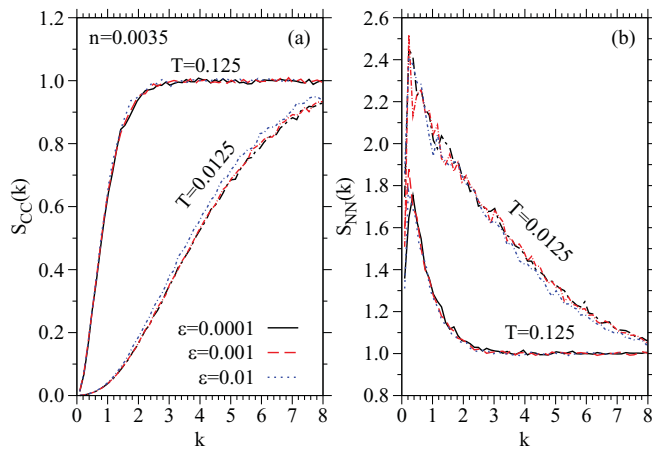J. Chem. Phys. **134**, 244514 (2011)

FIG. 19. (a) Concentration-concentration structure factors $S_{CC}(k)$ and (b) number-number structure factors $S_{NN}(k)$ at $n = 0.0035$ and different temperatures (as labeled), obtained using different values of the Ewald sum precision ε: $\varepsilon = 10^{-4}$ (full lines), $\varepsilon = 10^{-3}$ (dashed lines), and $\varepsilon = 10^{-2}$ (dotted lines).

a consequence, a large cutoff must be employed to evaluate the real space contribution U_r. Therefore, complete splitting of the interaction into real space and Fourier space contributions does not appear particularly convenient for the system at hand.

MD simulations were carried out in the microcanonical ensemble (NVE) using the velocity Verlet algorithm with a time step $\delta t = 0.08$. Equilibration at the temperature of interest was achieved by coupling the system to a massively stochastic heat bath.[54] Monte Carlo simulations have been performed in the canonical (NVT) and grand-canonical (μVT) ensemble. To accelerate equilibration at low density and temperature, we also implemented cluster moves to displace and insert/delete pairs of ions, as described in Ref. 40. In NVT simulations, the maximal displacements of standard displacement moves and cluster moves were adjusted during equilibration so as to keep the acceptance ratio around 30%. In μVT simulations, both random and biased insertions/deletions of pairs were attempted, together with standard displacement and cluster moves. Analysis of the acceptance ratios of Monte Carlo moves as a function of state parameters showed that biased insertions/deletions become favorable close to the estimated critical region, as expected. Proper equilibration of the system at low density was checked by comparing results of different thermal histories and different simulation methods. We remark that equilibration may become a serious issue at densities and temperatures lower than the ones considered in this work. In that case, more efficient simulation methods should be used.[37]

APPENDIX B: EFFECTIVE INTERACTIONS

In this Appendix, a brief derivation is provided for the effective interaction between two anion/cation pairs, and between a free ion and a pair, in the limit of large separations. Consider first the case of two pairs. Let $\mathbf{r}_1$ and $\mathbf{r}_2$ denote the distances between the two oppositely charged polyions in the two pairs, and let $\mathbf{R}$ be the vector joining the CM's of the

pairs. For sufficiently low temperatures T, the classical relative vibrations of the two ions in a pair are of small amplitude, so that their interaction potential $v_{+-}(r)$ may be replaced by its small r limit (Eq. (10)), i.e., $\beta v_{+-}(r) = -\beta u + \frac{\gamma}{2} r^2$ with $u = Q^2/(\sqrt{\pi}\epsilon'\sigma)$ and $\gamma = \beta u/6\sigma^2$. The configurational part of the internal partition function of an isolated pair is hence

$$q_1 = e^{\beta u} \int e^{-\gamma r^2/2} d\mathbf{r} = e^{\beta u} \frac{(2\pi)^{3/2}}{\gamma^{3/2}}. \tag{B1}$$

The configurational part of the partition function of two interacting pairs separated by $\mathbf{R}$ is

$$q_2(R) = \int d\mathbf{r}_1 \int d\mathbf{r}_2 \exp\left\{-\beta\big[v_{+-}(r_1)\right.$$
$$\left. + v_{+-}(r_2) + v_{12}(\mathbf{R}, \mathbf{r}_1, \mathbf{r}_2)\big]\right\}. \tag{B2}$$

If $R \gg \sigma$, one may adopt the point dipole approximation for the pair/pair interaction, each carrying a dipole $\mathbf{m}_i = Q\mathbf{r}_i$

$$\beta v_{12}(\mathbf{R}, \mathbf{r}_1, \mathbf{r}_2) = \frac{\beta Q^2}{\epsilon'}\left[\frac{\mathbf{r}_1 \cdot \mathbf{r}_2}{R^3} - \frac{3(\mathbf{R} \cdot \mathbf{r}_1)(\mathbf{R} \cdot \mathbf{r}_2)}{R^5}\right]. \tag{B3}$$

Substituting Eq. (B3) into Eq. (B2), and choosing $\mathbf{R}$ to be the polar axis, q_2 may be cast in the form

$$q_2(R) = 2\pi e^{2\beta u} \int_0^\infty e^{-\gamma r_1^2/2} r_1^2 dr_1 \int_0^\infty e^{-\gamma r_2^2/2} r_2^2 dr_2$$
$$\times \int_0^{2\pi} d\varphi \int_0^\pi \sin\Theta_1 d\Theta_1 \int_0^\pi \sin\Theta_2 d\Theta_2$$
$$\times \exp\left\{-\frac{\beta Q^2}{\epsilon'}\frac{r_1 r_2}{R^3}[\sin\Theta_1 \sin\Theta_2 \cos\varphi\right.$$
$$\left. - 2\cos\Theta_1 \cos\Theta_2]\right\}, \tag{B4}$$

where $\varphi = \varphi_1 - \varphi_2$. For sufficiently large R, the last exponential in the integrand of Eq. (B4) may be Taylor expanded. Elementary calculations show that all odd power terms in the expansion vanish upon carrying out the angular integrations. Retaining the zeroth and second order terms in the Taylor expansion, one arrives at

$$q_2(R) = e^{2\beta u}\frac{(2\pi)^3}{\gamma^3}\left[1 + 108\pi\left(\frac{\sigma}{R}\right)^6\right]. \tag{B5}$$

The effective pair-pair potential is then given by the free energy of the interacting pairs minus the sum of the internal free energies of each pair, i.e.,

$$\beta v_{2,2}(R) = \beta f_2(R) = -\ln\left[\frac{q_2(R)}{(q_1)^2}\right]$$
$$= -\ln\left[1 + 108\pi\left(\frac{\sigma}{R}\right)^6\right] \simeq -108\pi\left(\frac{\sigma}{R}\right)^6, \tag{B6}$$

valid for $R \gg \sigma$. The "van der Waals" exponent 6 agrees with the asymptotic form of the effective potential extracted from MC simulations (Fig. 12). The next contribution would be $\mathcal{O}(1/R^{12})$.

Downloaded 30 Jun 2011 to 162.38.150.128. Redistribution subject to AIP license or copyright; see http://jcp.aip.org/about/rights_and_permissions

The effective ion/pair potential $v_{1,2}(R)$ may be calculated along similar lines, starting from the coupling between a single ion and a pair of instantaneous dipole moment $Q\mathbf{r}$:

$$\beta v(\mathbf{R}, \mathbf{r}) = \frac{\beta Q^2}{\epsilon'} \mathbf{R} \cdot \mathbf{r}. \tag{B7}$$

The resulting effective pair potential is found to be

$$\beta v_{1,2}(R) = -\frac{3\pi}{T} \left(\frac{\sigma}{R}\right)^4. \tag{B8}$$

Note that, contrary to $\beta v_{2,2}(R)$ in Eq. (B6), $\beta v_{1,2}(R)$ depends on temperature. The same calculation leads to the following expression for the reduced polarizability of an anion/cation pair:

$$\frac{\xi}{\sigma^3} = 6\sqrt{\pi}\epsilon'. \tag{B9}$$

[1] G. Gouy, J. Phys. **9**, 457 (1910).

[2] D. L. Chapman, Philos. Mag. **25**, 475 (1913).

[3] P. W. Debye and E. Hückel, Phys. Z. **24**, 185 (1923).

[4] N. Bjerrum, Kgl. Dan. Vidensk. Selsk. Mat.-Fys. Medd. **7**, 1 (1926).

[5] G. Stell, K. C. Wu, and B. Larsen, Phys. Rev. Lett. **37**, 1369 (1976).

[6] A. Z. Panagiotopoulos, J. Phys.: Condens. Matter **17**, S3205 (2005).

[7] J.-P. Hansen and H. Löwen, Annu. Rev. Phys. Chem. **51**, 209 (2000).

[8] R. van Roij, M. Dijkstra, and J.-P. Hansen, Phys. Rev. E **59**, 2010 (1999).

[9] M. E. Leunissen, C. G. Christova, A.-P. Hynninen, C. P. Royall, A. I. Campbell, A. Imhof, M. Dijkstra, R. van Roij, and A. van Blaaderen, Nature (London) **437**, 235 (2005).

[10] J. Ryden, M. Ullner, and P. Linse, J. Chem. Phys. **123**, 034909 (2005).

[11] V. Dahirel and J.-P. Hansen, J. Chem. Phys. **131**, 084902 (2009).

[12] A.-P. Hynninen, M. E. Leunissen, A. van Blaaderen, and M. Dijkstra, Phys. Rev. Lett. **96**, 018303 (2006).

[13] J. B. Caballero, E. G. Noya, and C. Vega, J. Chem. Phys. **127**, 244910 (2007).

[14] E. Sanz, M. E. Leunissen, A. Fortini, A. van Blaaderen, and M. Dijkstra, J. Phys. Chem. B **112**, 10861 (2008).

[15] J.-L. Barrat and J. F. Joanny, Adv. Chem. Phys. **94**, 1 (1995).

[16] B. Philipp, H. Dautzenberg, K. J. Linov, J. Kötz, and W. Davydoff, Prog. Polym. Sci. **14**, 91 (1989).

[17] E. Tsuchida, J. M. S,-Pure Appl. Chem. A **31**, 1 (1994).

[18] H. Dautzenberg, Macromolecules **30**, 7810 (1997).

[19] H.-M. Buchhammer, M. Mende, and M. Oelmann, Colloids Surf., A **218**, 151 (2003).

[20] S. F. Edwards, Proc. Phys. Soc. London **85**, 613 (1965).

[21] G. H. Fredrickson, *The Equilibrium Theory of Inhomogeneous Polymers* (Oxford University Press, New York, 2006).

[22] M. Castelnovo and J. F. Joanny, Eur. Phys. J. E **6**, 377 (2001).

[23] J. Lee, Y. O. Popov, and G. H. Fredrickson, J. Chem. Phys. **128**, 224908 (2008).

[24] A. Y. Grosberg, P. G. Khalatur, and A. R. Khoklov, Mater. Chem. Phys. **3**, 709 (1982).

[25] J. Dautenhahn and C. K. Hall, Macromolecules **27**, 5399 (1994).

[26] P. G. Bolhuis, A. A. Louis, J.-P. Hansen, and E. J. Meijer, J. Chem. Phys. **114**, 4296 (2001).

[27] Y. Levin and M. E. Fisher, Physica A. **225**, 164 (1996).

[28] C. Valeriani, P. J. Camp, J. W. Zwanikken, R. van Roij, and M. Dijkstra, Soft Matter **6**, 2793 (2010).

[29] D. Coslovich, J.-P. Hansen, and G. Kahl, Soft Matter **7**, 1690 (2011).

[30] M. Baus and J.-P. Hansen, Phys. Rep. **59**, 1 (1980).

[31] F. H. Stillinger and R. Lovett, J. Chem. Phys. **48**, 3858 (1968).

[32] M. J. Gillan, Mol. Phys. **49**, 421 (1983).

[33] D. Ruelle, *Statistical Mechanics: Rigorous Results* (World Scientific, Singapore, 1999).

[34] J.-P. Hansen and I. R. McDonald, Phys. Rev. A **23**, 2041 (1981).

[35] J.-P. Hansen and I. R. McDonald, *Theory of Simple Liquids*, 3rd ed. (Academic, New York, 2006).

[36] J. Kirkwood, J. Chem. Phys. **3**, 300 (1935).

[37] C. Valeriani, P. J. Camp, J. W. Zwanikken, R. van Roij, and M. Dijkstra, J. Phys.: Condens. Matter **22**, 104122 (2010).

[38] M. Fisher and S. Fishman, Phys. Rev. Lett. **47**, 421 (1981).

[39] L. Belloni, J. Chem. Phys. **98**, 8080 (1993).

[40] G. Orkoulas and A. Z. Panagiotopoulos, J. Chem. Phys. **101**, 1452 (1994).

[41] B. Widom, J. Chem. Phys. **39**, 2808 (1963).

[42] J. Kirkwood, J. Chem. Phys. **7**, 911 (1939).

[43] M. Neumann, Mol. Phys. **50**, 841 (1983).

[44] E. Luijten, M. E. Fisher, and A. Z. Panagiotopoulos, Phys. Rev. Lett. **88**, 185701 (2002).

[45] J.-M. Caillol, D. Levesque, and J.-J. Weis, J. Chem. Phys. **116**, 10794 (2002).

[46] J. M. Romero-Enrique, L. F. Rull, and A. Z. Panagiotopoulos, Phys. Rev. E **66**, 041204 (2002).

[47] J. Kosterlitz and D. Thouless, J. Phys. C **6**, 1181 (1973).

[48] J.-M. Caillol and D. Levesque, Phys. Rev. B **33**, 499 (1986).

[49] G. Orkoulas and A. Z. Panagiotopoulos, J. Chem. Phys. **104**, 7206 (1996).

[50] Y. Levin, X. J. Li, and M. E. Fisher, Phys. Rev. Lett. **73**, 2716 (1994).

[51] N. B. Wilding, Am. J. Phys. **69**, 1147 (2001).

[52] D. Frenkel and B. Smit, *Understanding Molecular Simulation* (Academic, New York, 2001).

[53] W. Smith and T. R. Forester, J. Mol. Graphics **14**, 136 (1996).

[54] M. P. Allen and D. J. Tildesley, *Computer Simulation of Liquids* (Clarendon, Oxford, 1987).